Transformation optics with Fabry-Pérot resonances

M. M. Sadeghi*, Sucheng Li*, Lin Xu*, Bo Hou [1], and Huanyang Chen [1]

College of Physics, Optoelectronics and Energy, Soochow University, Suzhou 215006, China

* These authors contributed equally to this work.

[1] Correspondence and requests for materials should be addressed to H.C. (chy@suda.edu.cn) or

B.H. (houbo@suda.edu.cn)

Supplementary Notes

Supplementary Note S1

In this supplementary note, we will analytically prove that for the following configuration, perfect transparency or invisibility could be achieved at the FP resonant conditions:

$\varepsilon = \mu = 1$, for $r \geq r_2$ (Region 1);

$\varepsilon_r = \infty$ and $\varepsilon_\theta = \mu_z = 1$, $r_1 \leq r < r_2$ (Region 2);   (S1)

$\varepsilon = \mu_z = \dfrac{r_2}{r_1}$, for $0 \leq r < r_1$ (Region 3).

We drop the primes here for aesthetic reasons. The magnetic field in Region 1 could be written as,

$$H_1^z(r, \theta) = \sum_n (a_n J_n(k_0 r) + b_n H_n^{(1)}(k_0 r)) e^{in\theta} ,$$ (S2)

where $k_0 = \dfrac{2\pi}{\lambda}$ is the wave-vector in vacuum (λ is the wavelength in vacuum), b_n are coefficients of the scattered field to be determined, a_n are coefficients of the incident field (for an incident plane wave in x-direction, $a_n = i^n$). J_n and $H_n^{(1)}$ are the n-th order Bessel Functions and Hankel Functions of the first kind. As $\varepsilon_r = \infty$, the magnetic field in Region 2 shall be written as,

$$H_2^z(r, \theta) = g J_0(k_0 r) + h Y_0(k_0 r) ,$$ (S3)

with only the monopole terms (J_0 and Y_0 are the zero-th order Bessel Function and Neumann Function). g and h are coefficients to be determined. For Region3, the magnetic field shall be written as,

$$H_3^z(r, \theta) = \sum_n (f_n J_n(\frac{r_2}{r_1} k_0 r)) e^{in\theta} ,$$ (S4)

where f_n are coefficients of the inner field to be determined. After matching the continual boundary conditions for H^z and E^θ at $r = r_1$ and $r = r_2$, we can eventually obtain,

$$b_n = a_n \frac{C_n J_n{}'(k_0 r_2) - D_n J_n(k_0 r_2)}{D_n H_n^{(1)}(k_0 r_2) - C_n H_n^{(1)}{}'(k_0 r_2)} ,$$ (S5)

where

$$C_n = \frac{J_1(k_0 r_1) Y_0(k_0 r_2) J_n(k_0 r_2) + J_0(k_0 r_1) Y_0(k_0 r_2) J_n{}'(k_0 r_2) - Y_1(k_0 r_1) J_0(k_0 r_2) J_n(k_0 r_2) - Y_0(k_0 r_1) J_0(k_0 r_2) J_n{}'(k_0 r_2)}{Y_0(k_0 r_1) J_1(k_0 r_1) - Y_1(k_0 r_1) J_0(k_0 r_1)}$$

(S6)

$$D_n = \frac{Y_1(k_0 r_1) J_1(k_0 r_2) J_n(k_0 r_2) + Y_0(k_0 r_1) J_1(k_0 r_2) J_n{}'(k_0 r_2) - J_1(k_0 r_1) Y_1(k_0 r_2) J_n(k_0 r_2) - J_0(k_0 r_1) Y_1(k_0 r_2) J_n{}'(k_0 r_2)}{Y_0(k_0 r_1) J_1(k_0 r_1) - Y_1(k_0 r_1) J_0(k_0 r_1)}$$

(S7)

We thereby plot the total scattering cross section $\sigma = \sum_n |b_n|^2$ as the function of wavelength for

an incident plane wave in x-direction and for the case of $r_1 = 1$ and $r_2 = 2$ in Supplementary Figure S13, where we find that almost zero scattering cross section could be achieved at around $\lambda = \dfrac{2}{m}$ ($m = 1, 2, 3...$). If we substitute the asymptotic forms of Bessel Functions, Neumann functions, and Hankel Functions of the first kind into Equation (S5), we will get exact zero value of b_n at $k_0(r_2 - r_1) = m\pi$, which is actually consistent with Equation (5) in the main text.

Supplementary Figures

The coaxial detector

The cylindrical sample

The horn antenna
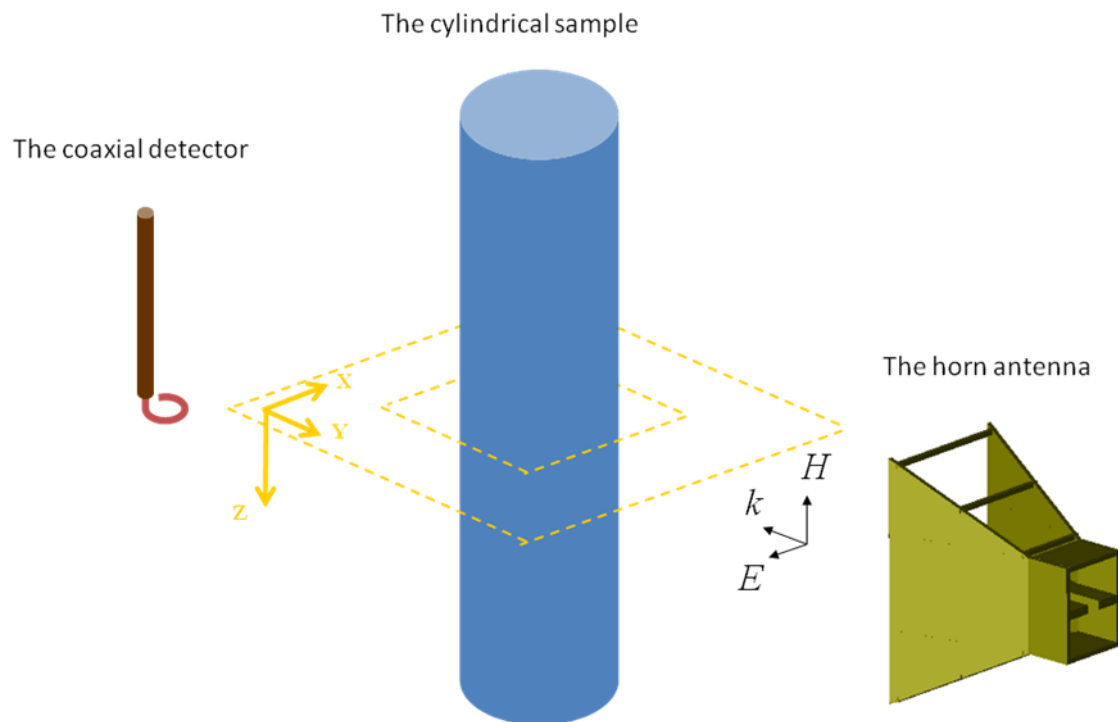
Supplementary Figure S1. The measurement setup. In the experiment, the samples are placed vertically with the cylindrical axis orientated along the *z*-direction, and a horn-shaped antenna, located ~*100 cm* away from the samples, transmits microwaves toward them with H-field polarized along the vertical direction. The scanning plane, measuring *300×300 mm²*, is located in the middle of the *500 mm* high samples to avoid the ending effect.
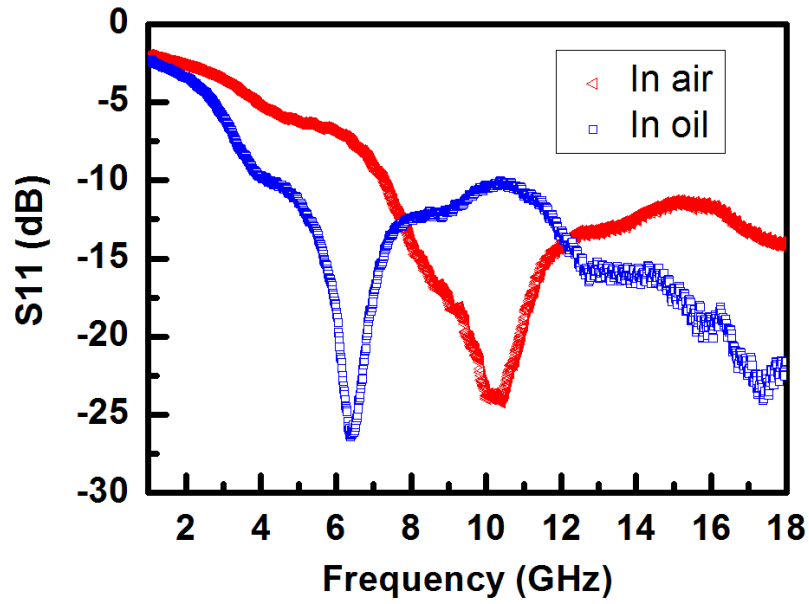
Supplementary Figure S2. The magnetic response of the detector. To map the spatial distribution of the H_z component, we employ a split ring detecting antenna which is made of a coaxial cable and has a circular loop of diameter *4 mm* and a split *1 mm*. Its *S11* parameter is characterized first to identify the magnetic response frequency which is shown around *10GHz* in air. When the detector is inserted into the oil, the overall spectrum will downshift, bringing about a change in the radiating/receiving capability of the detector at each specific frequency, for example, one of our working frequencies (*9.35GHz*). Thus, the scanned field magnitude inside the oil cylinder needs to be corrected to make the direct comparison with the external fields in air.
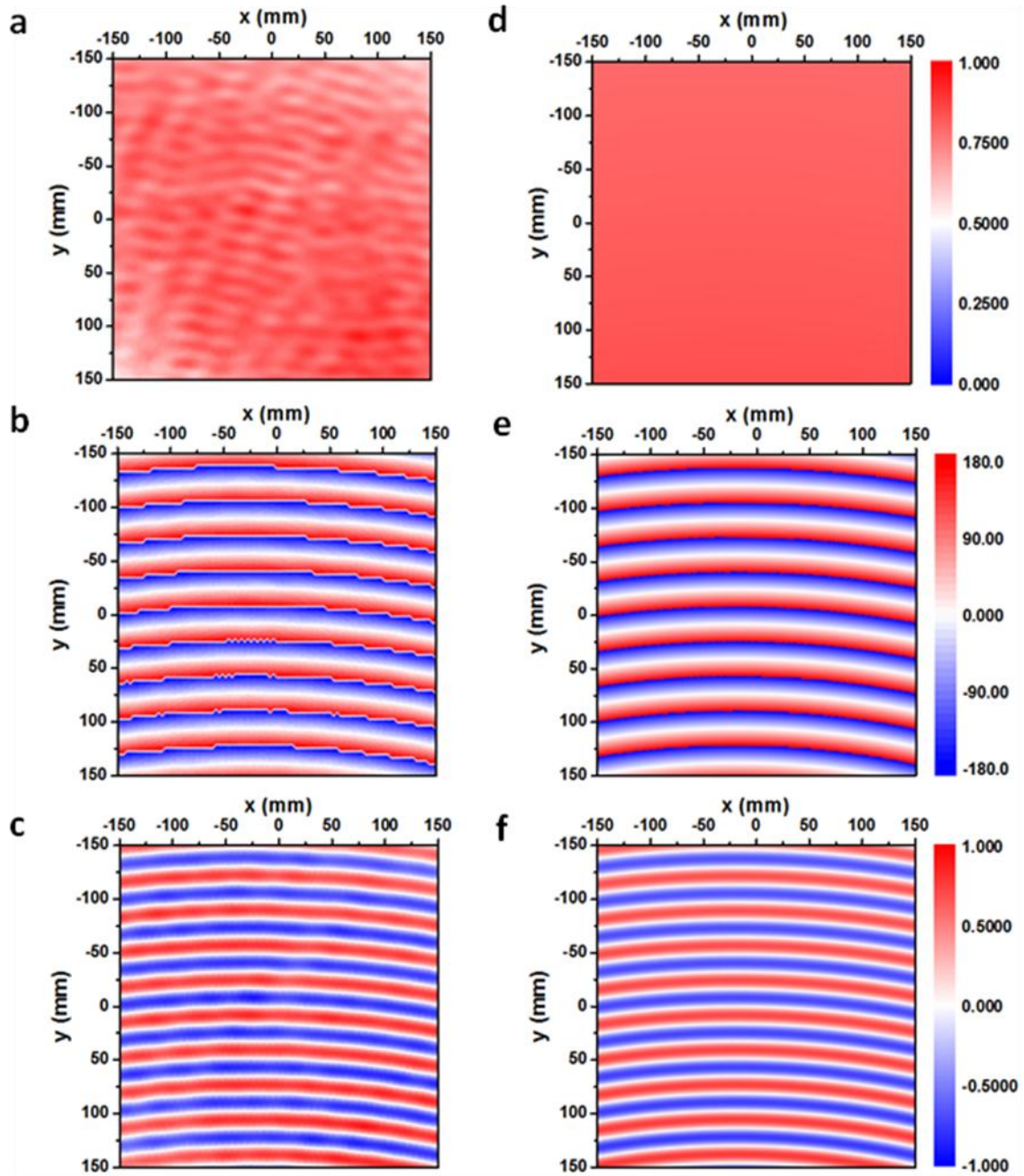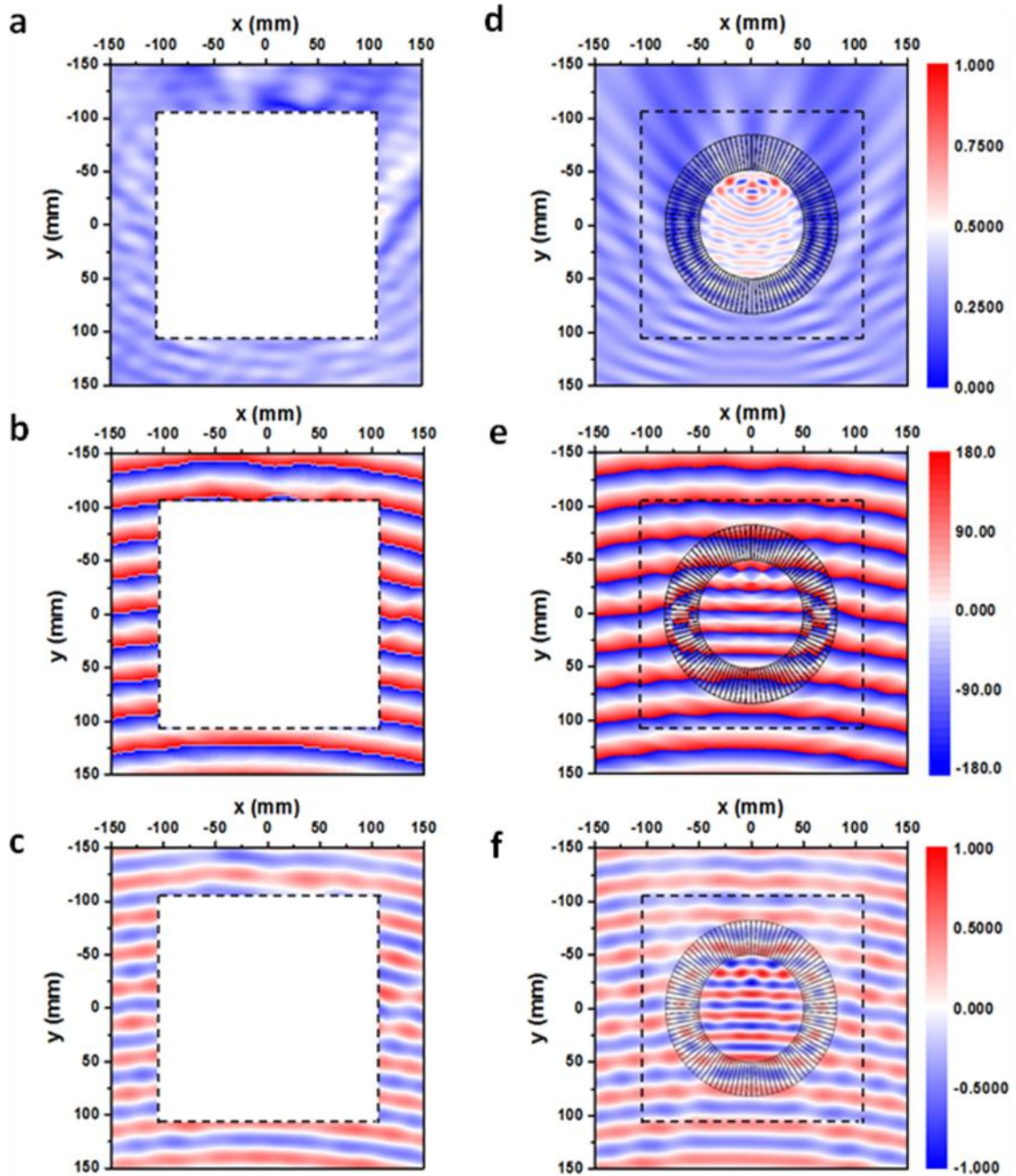
Supplementary Figure S3. The incident H-field at *9.26GHz* in free space. (a), The magnitude of the measured field; (b), The phase of the measured field; (c), The real part of the measured field; (d), The magnitude of the simulated field; (e), The phase of the simulated field; (f), The real part of the simulated field. It is seen that the field is incident toward the *-y* direction and has the quasi-plane wave feature with slightly curved wavefronts.
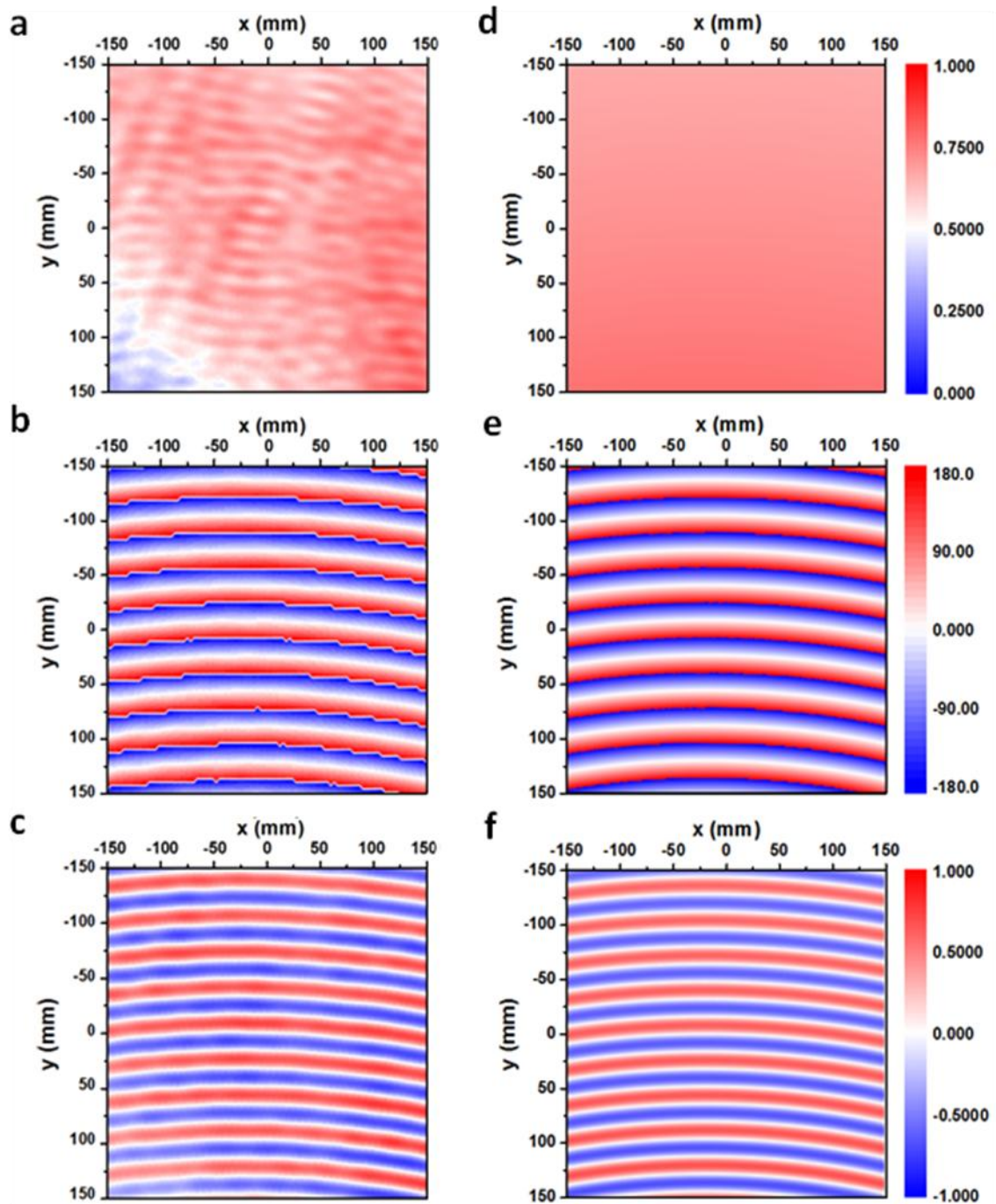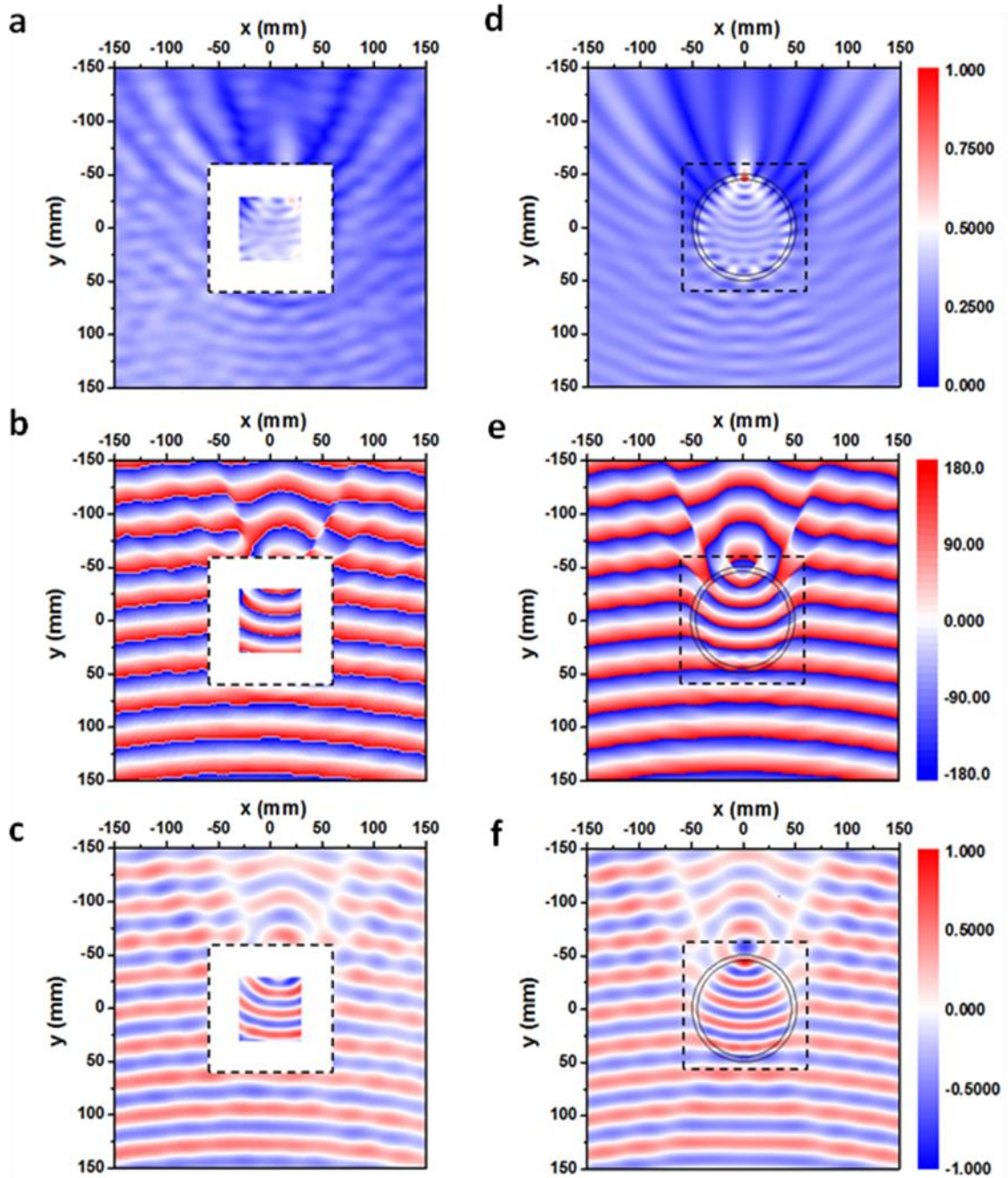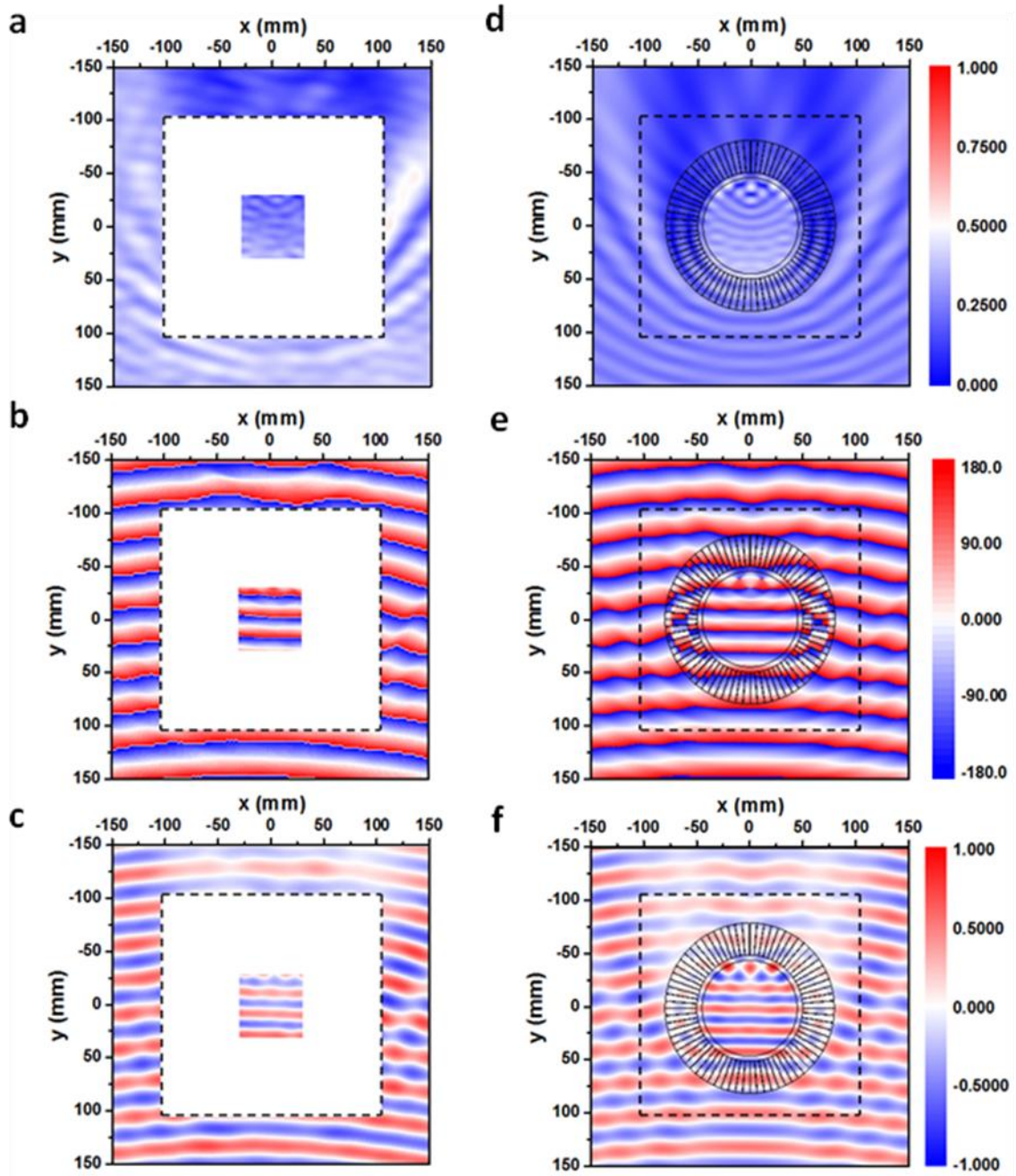
Supplementary Figure S4. The incident H-field at *9.35GHz* in free space. (a), The magnitude of the measured field; (b), The phase of the measured field; (c), The real part of the measured field; (d), The magnitude of the simulated field; (e), The phase of the simulated field; (f), The real part of the simulated field.
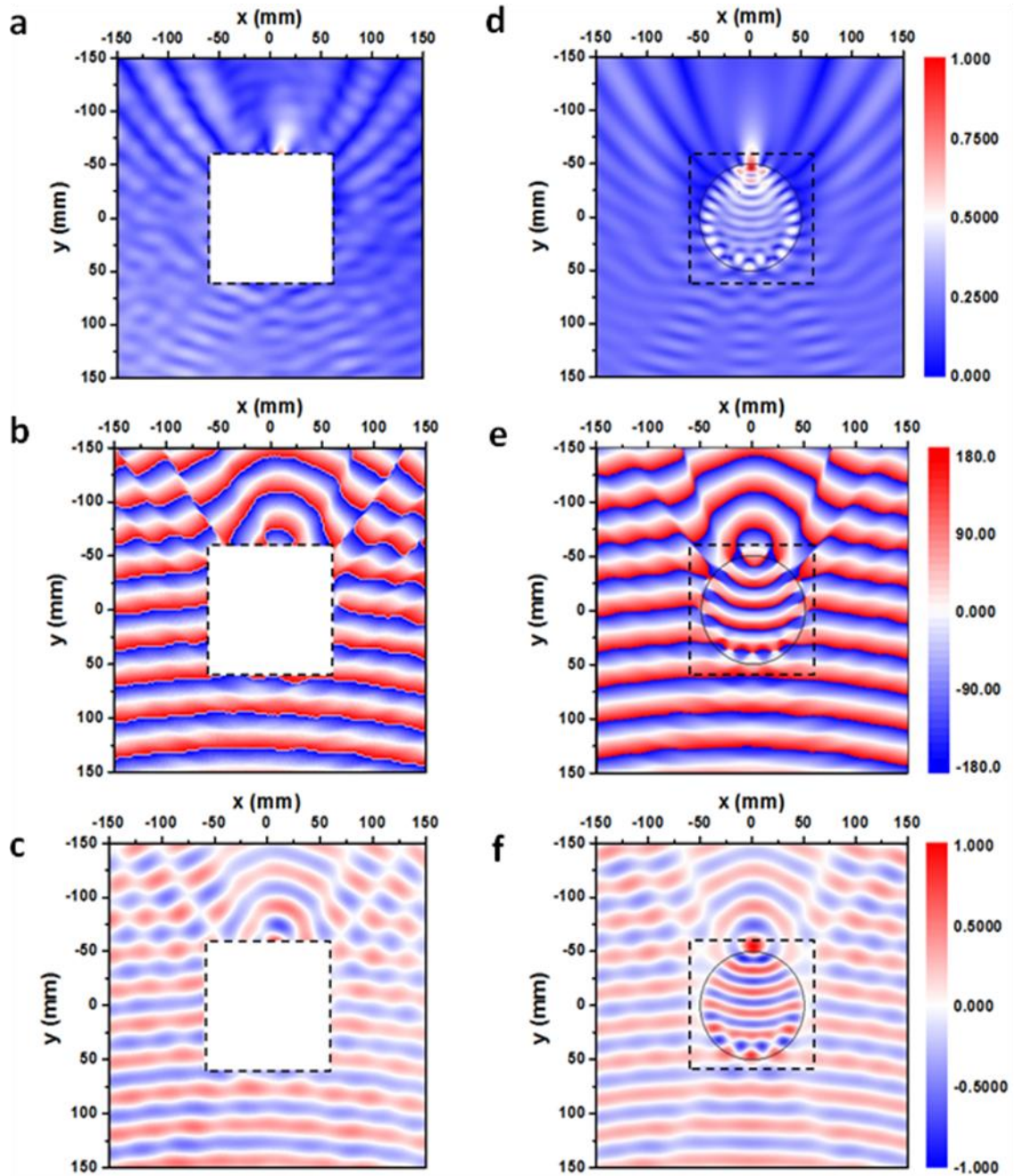
Supplementary Figure S5. The H-field of the solid Plexiglas cylinder at *9.26GHz*. (a), The magnitude of the measured field; (b), The phase of the measured field; (c), The real part of the measured field; (d), The magnitude of the simulated field; (e), The phase of the simulated field; (f), The real part of the simulated field.

Supplementary Figure S6. The H-field of the concentrator with the solid Plexiglas cylinder at *9.26GHz*. (a), The magnitude of the measured field; (b), The phase of the measured field; (c), The real part of the measured field; (d), The magnitude of the simulated field; (e), The phase of the simulated field; (f), The real part of the simulated field.

Supplementary Figure S7. The H-field of the oil cylinder at *9.35GHz*. (a), The magnitude of the measured field; (b), The phase of the measured field; (c), The real part of the measured field; (d), The magnitude of the simulated field; (e), The phase of the simulated field; (f), The real part of the simulated field.

Supplementary Figure S8. The H-field of the concentrator with the oil cylinder at *9.35GHz*. (a), The magnitude of the measured field; (b), The phase of the measured field; (c), The real part of the measured field; (d), The magnitude of the simulated field; (e), The phase of the simulated field; (f), The real part of the simulated field.
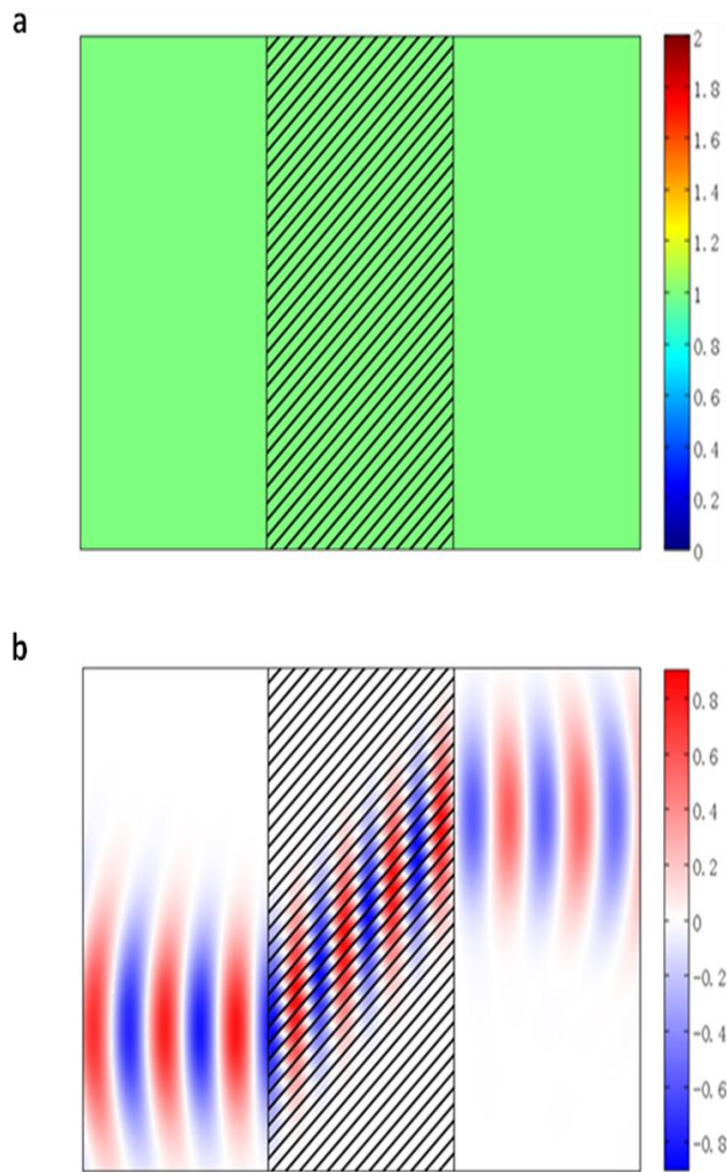
Supplementary Figure S9. The shifter with FP resonance. (a), The refractive index profile; (b), The shifting functionality.
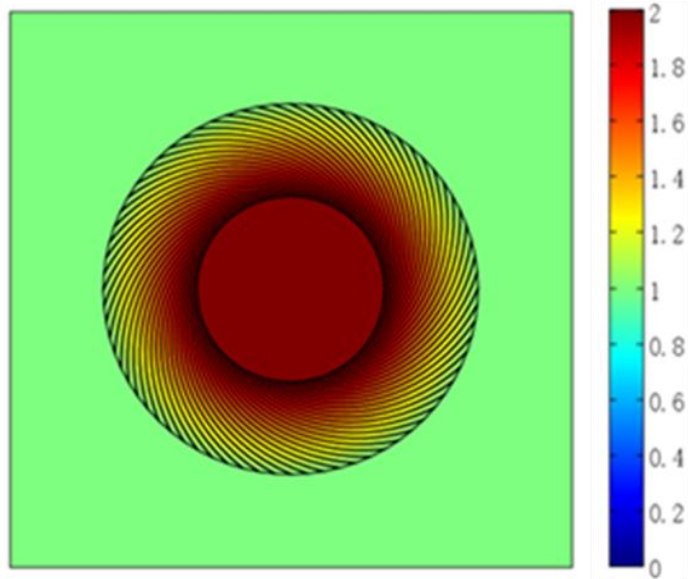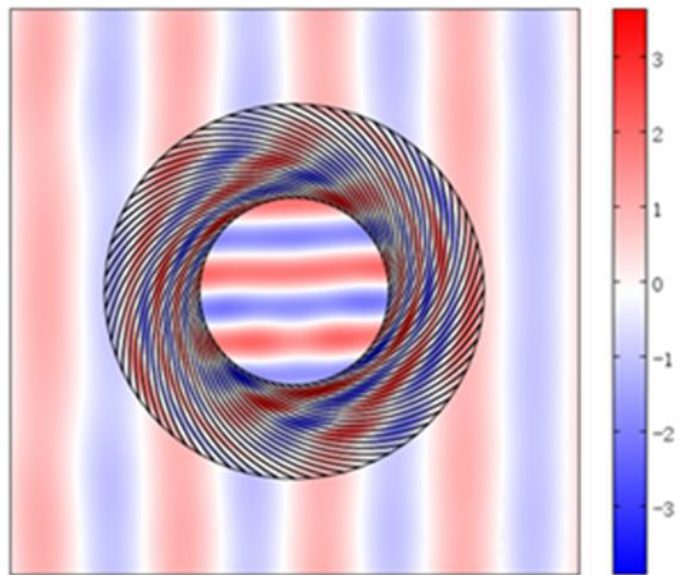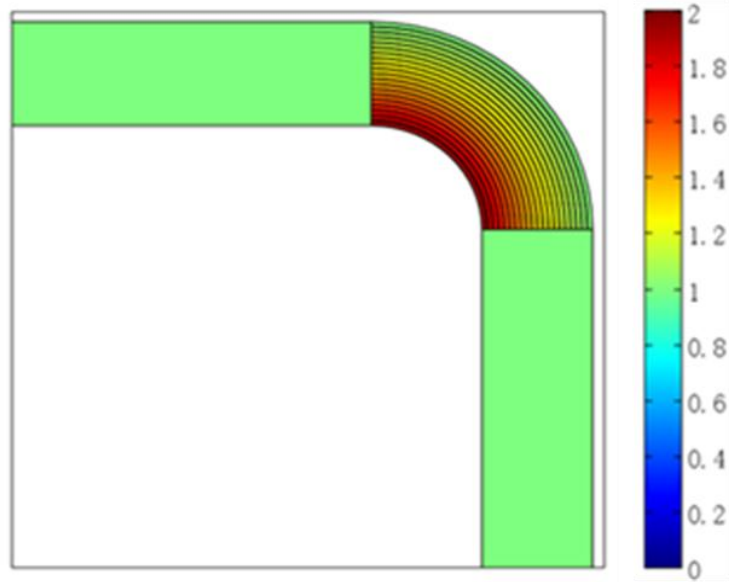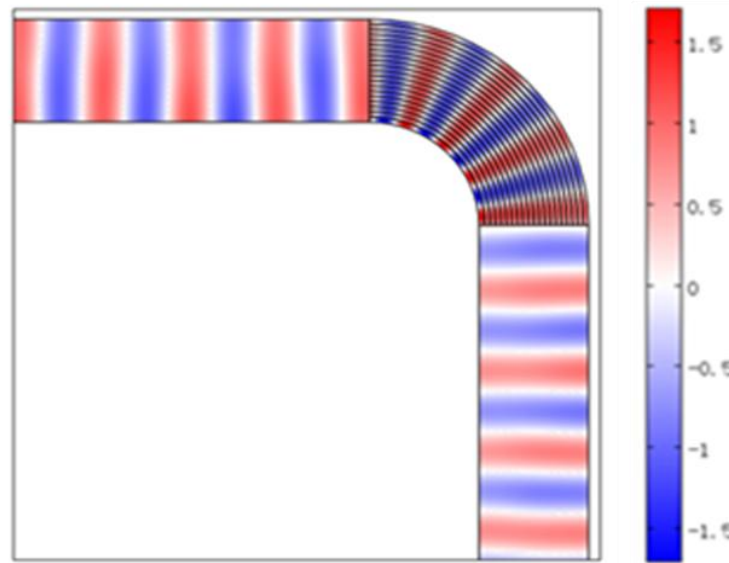
Supplementary Figure S10. The rotator with FP resonance. (a), The refractive index profile; (b), The wavefront rotation functionality.
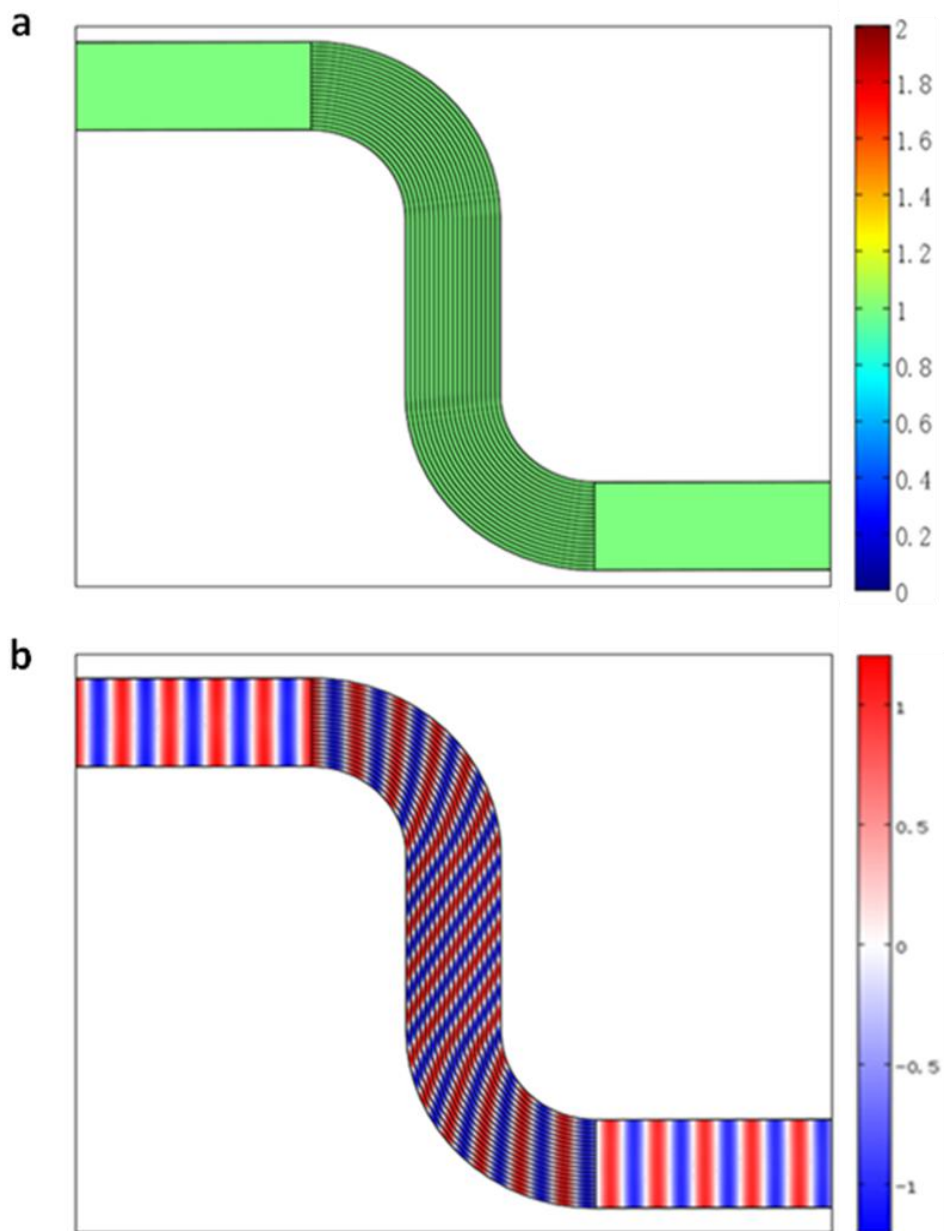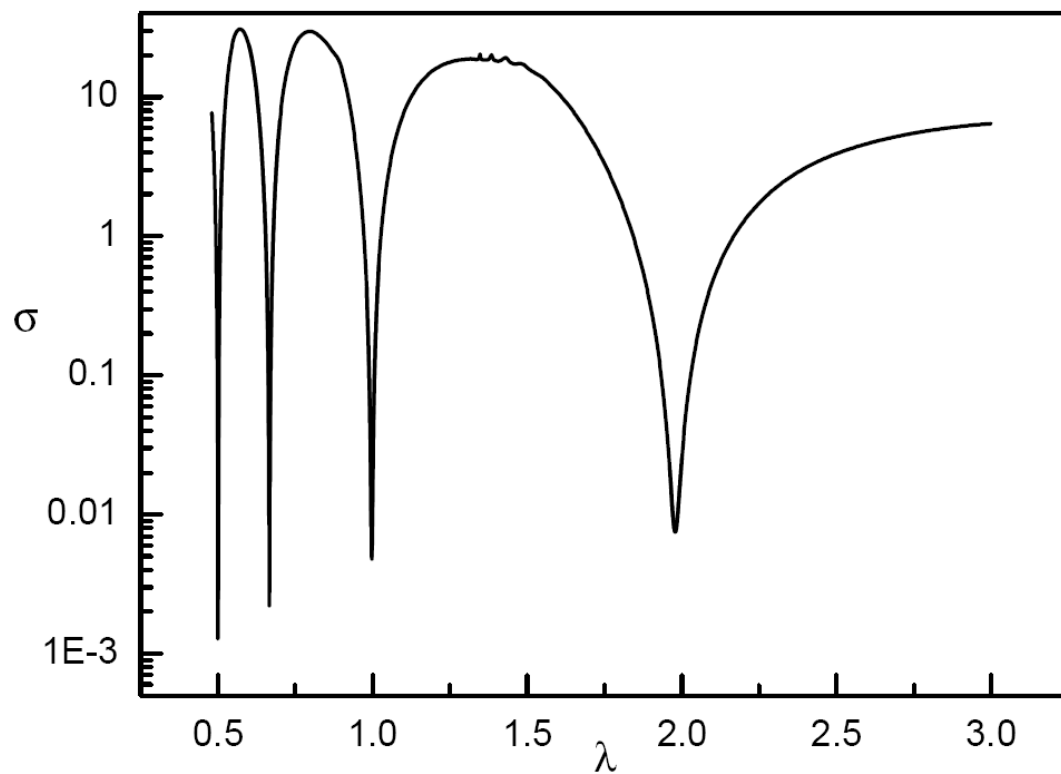
Supplementary Figure S11. The waveguide bend with FP resonance. (a), The refractive index profile; (b), The wave bending functionality.

Supplementary Figure S12. The waveguide periscope with FP resonance. (a), The refractive index profile; (b), The periscope functionality.

Supplementary Figure S13. The total scattering cross section as the function of wavelength.